AIAA JOURNAL
Vol. 49, No. 2, February 2011

Blowing Effects on the Separated Flow over a Moderately Swept Missile Fin

Jacques Riou* and Eric Garnier*
ONERA, 92190 Meudon, France
and
Claude Basdevant†
Université Paris 13, 93430 Villetaneuse, France

DOI: 10.2514/1.J050082

This aim of this numerical study is to control the separated flow over a generic missile fin characterized by a sweep angle of 50 deg and a sharp leading edge. The flow without control separates at the leading edge and the fin is stalled. To control the flow separation, a blowing slot is placed all along the fin leading edge, and both continuous and pulsed blowing are applied. The nondimensional frequencies F^+ based on the freestream velocity and the root chord of the fin are equal to 1, 1.5, 3, 6, and 10. Applying continuous blowing results in a larger reverse-flow region than in the reference case. As a consequence, the aerodynamic performance of the fin is deteriorated. Conversely, using pulsed blowing tends to decrease the pressure over the fin and the extent of the reverse-flow region. The performance of the fin is then enhanced, particularly for a pulsing frequency equal to that of natural vortex-shedding ($F^+ = 1.5$). Finally, the last part of the paper discusses the effects of the suction phase by comparing synthetic-jet actuation and pulsed blowing at the optimal frequency.

Nomenclature

b	=	local span
C_D	=	drag coefficient
C_L	=	lift coefficient
C_p	=	pressure coefficient
C_μ	=	momentum coefficient
c	=	root chord of the fin
F^+	=	nondimensional frequency
$G(f)$	=	spectral power density
$G_v(f)$	=	power spectral density
M_∞	=	freestream Mach number
Re_c	=	Reynolds number
S_{fin}	=	surface of the fin
St_c	=	Strouhal number
U_∞	=	freestream velocity
x_c	=	longitudinal location nondimensionalized by c
x_{cp}	=	longitudinal position of the aerodynamic center of pressure
z_{cp}	=	lateral position of the aerodynamic center of pressure
α	=	angle of attack
ψ	=	sweep angle
σ	=	standard deviation

I. Introduction

THE flow over moderately swept delta wings (with sweep angle ψ varying from 45 to 55 deg) is a recent topic of interest, mostly because of their application to military aircraft and unmanned combat air vehicles. The flow over such wings presents, to some extent, analogies with the flow that develops over highly swept wings ($\psi > 55°$). The flow coming from the lower surface of the wing separates at the leading edge, resulting in a curved shear layer that rolls up, creating the leading-edge vortex. The longitudinal flow in the vortex core is characterized by an acceleration, the ratio u/U_∞ reaching values as high as 3 [1,2]. This acceleration of the longitudinal flow in the vortex core leads to a pressure decrease that generates an additional lift force [3,4]. However, as the angle of attack increases, the vortex undergoes a sudden disorganization known as vortex breakdown [5–7]. The latter is characterized by the dilatation of the vortex core and a sudden decrease of the longitudinal velocity. The position of the vortex breakdown progresses toward the apex of the wing as the angle of attack increases; for large angles of attack, the flow becomes fully separated and the wing stalls. Independently from these common features with highly swept wings, the vortical flow over moderately swept delta wings presents some specificities. It has been observed that the vortex develops at lower incidence than for highly swept wings. The vortex breakdown also occurs earlier and can consequently reach the apex for moderate angles of attack [8–10]. It results in an anticipated full separation, in comparison with the case of slender delta wings [11,12]. Thus, from an industrial point of view, delaying moderately swept delta-wing stall is a challenge aimed at increasing the application domain of such wings. It has been experimentally demonstrated that blowing at the leading edge of wings can control flow separation [13]. Moreover, the experimental works of Williams et al. [14] have shown that in the case of a pulsed blowing imposed along the leading edge of a 50 deg swept wing, the optimal frequency delaying the stall is close to $F^+ = 1.5$, where F^+ is the nondimensional blowing frequency based on the freestream velocity and the root chord of the wing. Nevertheless, both the Reynolds number and Mach number of this study are low, and fluidic control efficiency is not yet documented in the transonic regime. Thus, the aim of the current study is to numerically evaluate the control efficiency in the case of a stalled moderately swept missile fin in the transonic regime and for a realistic Reynolds number. Another objective of the study is to compare continuous, pulsed, and synthetic-jet effects on the flow developing over stalled moderately swept wings and to discuss the blowing-frequency effects on the control efficiency. The computations presented in the current study are carried out using a coupling of delayed-detached-eddy simulation (DDES) [15] and zonal-detached-eddy simulation (ZDES) [16] methods. This study is a follow-up of [17], where the capability of this method computing the uncontrolled flow has been demonstrated. Nevertheless, in order to decrease the numerical dissipation, the AUSM scheme is preferred to the Roe scheme in the current study. Furthermore, the integration time is increased from

Received 22 July 2009; revision received 21 September 2010; accepted for publication 21 October 2010. Copyright © 2010 by the American Institute of Aeronautics and Astronautics, Inc. All rights reserved. Copies of this paper may be made for personal or internal use, on condition that the copier pay the $10.00 per-copy fee to the Copyright Clearance Center, Inc., 222 Rosewood Drive, Danvers, MA 01923; include the code 0001-1452/11 and $10.00 in correspondence with the CCC.

*Research Engineer, Applied Aerodynamics Department, 8 rue des Vertugadins.
†Professor, Institut Galilée, 99 Avenue J.B. Clément.

$5c/U_\infty$ to $20c/U_\infty$ in order to enhance the description of the low-frequency phenomena.

The paper is organized as follows. Section II describes the test case, and Sec. III presents the turbulent modeling and the mesh used in the study. Then the reference case is presented in Sec. IV. It focuses, in particular, on the spectral analysis of the vertical velocity that highlights the frequencies of the natural phenomena present in the separated flow. These frequencies are used to set those of the pulsed blowing. Section V then presents the effects of continuous and pulsed blowing on the separated flow and on the aerodynamic performance of the missile fin. Finally, Section VI is dedicated to the comparison between the synthetic-jet actuation and the pulsed one at $F^+ = 1.5$.

II. Test-Case Description

The missile fin chosen in this study can be considered as a 50 deg sweep delta wing with a sharp leading edge (see Fig. 1). The root chord of this fin is $c = 0.285$ m and the maximal span is 0.19 m. Moreover, in the experimental setup, the fin is mounted on a vertical plate to preserve the flow around the fin from the interaction with boundary layers developing on the wind-tunnel walls. To respect the experimental configuration as much as possible, this vertical plate is considered in the computational simulations. Additionally, the 0.5 mm slot between the vertical plate and the fin is also taken into account.

Concerning the reference case, all of the experimental data presented in this paper were acquired in ONERA's transonic wind tunnel S3MA at operating conditions of $M_\infty = 0.7$, $U_\infty = 226.5\ \mathrm{m \cdot s^{-1}}$, $P_{i\infty} = 1.5$ bar, and $T_{i\infty} = 278$ K and for angles of attack ranging from -2 to 40 deg [18]. The Reynolds number based on the root chord and freestream velocity is equal to $Re_c = 5.8 \times 10^6$. The fin has been painted with pressure-sensitive paint, giving the distribution of pressure on the suction side of the missile fin. Furthermore, the aerodynamic loadings and moments have been measured. The $\alpha = 25°$ case has been chosen because it corresponds to the angle of attack for which the fin is fully stalled.

III. Numerical Procedure

A. FLU3M Solver

The computations presented in this paper have been performed using the FLU3M solver, developed by ONERA [19]. This code is based on a cell-centered finite volume technique and structured multiblock meshes. For efficiency, an implicit time integration is employed to deal with the very small grid size encountered near the wall. The time integration is carried out by means of the second-order-accurate backward scheme of Gear [20], and the time step is set equal to 2.6×10^{-7} s. Moreover, four subiterations are used in the Newton integration. The spatial scheme is that proposed by Mary et al. [21]. It is based on the AUSM+(P) scheme, whose dissipation is proportional to the local fluid velocity. Furthermore, a second-order-accurate centered scheme is used to compute the viscous fluxes. The accuracy of the solver for direct numerical simulation, large-eddy simulation (LES), and hybrid Reynolds-averaged Navier–Stokes with LES has been assessed in various applications, including flows around a bidimensional airfoil in near-stall conditions [22], afterbody flows [23–25], cavity flows [26], and synthetic jets in a crossflow [27,28].

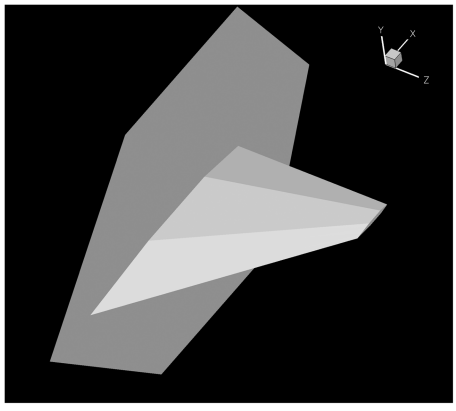

Fig. 1 Perspective view of the missile fin.

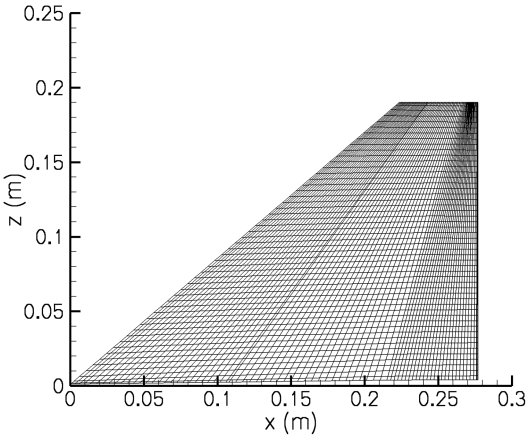

Fig. 2 Mesh of the suction side of the fin (one point every four, in each direction).

B. Turbulent Modeling

Because of the high Reynolds number of the flow preventing the use of LES, a hybrid RANS/LES method has been chosen to carry out the simulations. The chosen technique [17] relies on a coupling of the DDES [15] and the ZDES [16] methods, and both are grounded on the Spalart–Allmaras model [29]. It has been demonstrated in the case of the currently studied missile fin that this method leads to a significant improvement in the description of the turbulent structures in LES zones and in the prediction of the time-averaged pressure coefficient on the suction side of the fin [17]. This approach has also been successfully applied to the study of the compressibility effects on the vortical flow over a delta wing [30] and to the control of this flow in the transonic regime [31].

C. Numerical Mesh

The numerical grid has been built with the ICEM Hexa meshing tool. This structured grid has an O topology. There are 21×10^6 points, and the mesh is locally refined in the region of the leading edge, in order to ensure a sufficient discretization of the shear layer. The mesh of the suction side of the fin is shown in Fig. 2. Following a grid sensitivity study presented in [17], the mesh has been proven to be fine enough to capture unsteady phenomena. It ensures maximal Courant–Friedrichs–Lewy values of 15 in LES regions with the chosen time step.

IV. Overview of the Baseline Case

The aim of this section is to present an overview of the reference case.

A. Validation of the Baseline Case

Figure 3 compares the distribution of the computed time-averaged pressure coefficient C_p with the experimental data. In this figure, the evolution of C_p as a function of the local span z is represented at several longitudinal positions: $x_c = 0.1$, 0.3 , 0.6, and 0.9.

At the first location ($x_c = 0.1$), a low-pressure peak reaching $C_p = -0.98$ is observable in the experimental data. The computation also predicts this peak, but its intensity is underestimated by 16%. Downstream from this position, the intensity of the low-pressure peak decreases with respect to the distance from the apex. Moreover, a quite satisfying prediction of C_p distribution is obtained with the computation. Thus, the computation ensures an accurate prediction of the pressure on the suction side of the missile fin. Table 1 compares

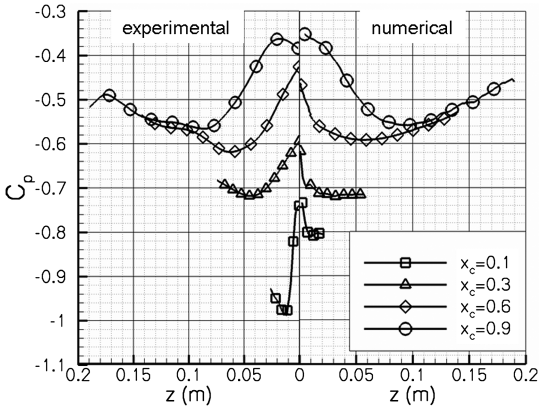

Fig. 3 Experimental and numerical repartition of C_p on the suction side of the fin.

experimental and numerical aerodynamic coefficients of the missile fin. The maximal error on the aerodynamic loading concerns the prediction of the lift coefficient, which is sufficiently accurate from an industrial application point of view, with less than 1.2% error. Moreover, the error on the position of the aerodynamic center of pressure remains lower than 1%. These observations indicate that the pressure distribution is not only well predicted on the upper surface, but also on the lower side of the fin. These results allow validation of the computation in regard to the available experimental data. It should also be emphasized that the use of the AUSM scheme instead of the Roe scheme allows a twofold reduction of the error level on the prediction of the aerodynamic performance of the fin and of the position of the aerodynamic center of pressure.

B. Presentation of the Instantaneous Flow

The purpose of this section is to present the instantaneous flow that develops over the missile fin. An efficient way to observe the turbulent structures is the Q criterion [32], defined as follows:

$$Q = -\tfrac{1}{2}(S_{ij}S_{ij} - \Omega_{ij}\Omega_{ij}) \tag{1}$$

In this equation, S and Ω, respectively, denote the strain rate and the rotation tensors. Figure 4 shows an isosurface of $Q = 400 \times U_\infty^2/c^2$.

As observable in Fig. 4, the flow detaches at the sharped leading edge of the fin, resulting in a three-dimensional separation area. In particular, at the early stage of the vortex-shedding at the leading edge of the fin, the vortical structures are two-dimensional and parallel to the leading edge and become three-dimensional as they are convected toward the trailing edge.

C. Overview on the Time-Averaged Flow

The averaging process has been performed over a physical time equal to 26 ms, which represents a duration of $20T_c$, where T_c is the time scale defined by $T_c = c/U_\infty$. The simulation cost approximately equals 1600 CPU hours distributed on two NEC SX8 processors. Figure 5 shows contours of u/U_∞ in several planes perpendicular to the surface of the missile fin. As it was predictable according to experimental observations of Ol and Gharib [11,12], a large region of reverse flow (in which the ratio u/U_∞ reaches -0.2) develops on the upper surface of the fin. At the apex of the fin, the lateral extension of this region equals the local span and becomes relatively less important as the distance from the apex increases. Furthermore, the longitudinal flow is accelerated between the

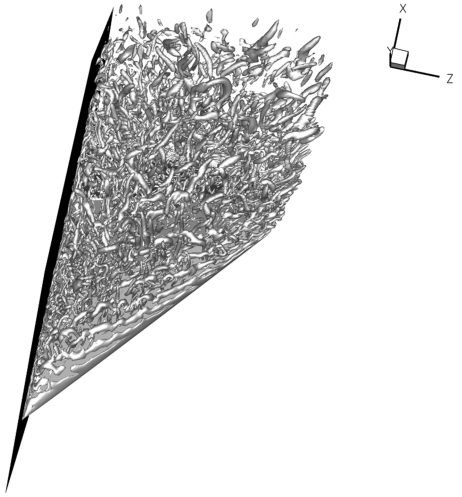

Fig. 4 Representation of the turbulent structures embedded in the separated flow.

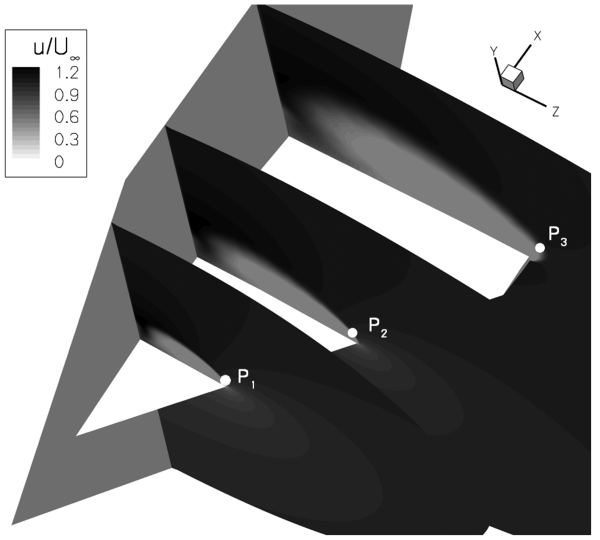

Fig. 5 Contours of u/U_∞ at $x/c = 0.3$, 0.5, and 0.9.

reverse-flow region and the vertical plate, and the local longitudinal velocity is equal to $1.2U_\infty(M = 0.85)$. Moreover, the flow coming from the lower surface bypasses the fin at the leading edge, imposing an important acceleration of the flow. It then results in an intense velocity gradient, leading to the formation of the previously observed vortical structures in the shear layer.

D. Spectral Analysis

To conclude this overview on the reference case, the spectral analysis of the resolved vertical velocity and pressure fluctuations (respectively, v' and p') is now presented. Such an analysis has been performed using the method of Welch [33]. Figure 6 shows spectra of the vertical velocity fluctuations v' at the longitudinal locations $x_c = 0.3(P_1), 0.5(P_2)$, and $0.9(P_3)$ at the leading edge of the missile fin. It corresponds to the region where the vortical structures embedded in the shear layer develop (see Fig. 5).

Table 1 Experimental and numerical aerodynamic performance of the fin

	C_L	C_D	x_{cp}	z_{cp}
Experiment	0.822	0.029	0.549	0.349
Riou et al. [17]	0.847 (+3%)	0.0294 (+1.3%)	0.558 (+1.7%)	0.352 (+0.94%)
Current investigation	0.832 (+1.2%)	0.02905 (<0.5%)	0.555 (+1%)	0.351(+0.5%)

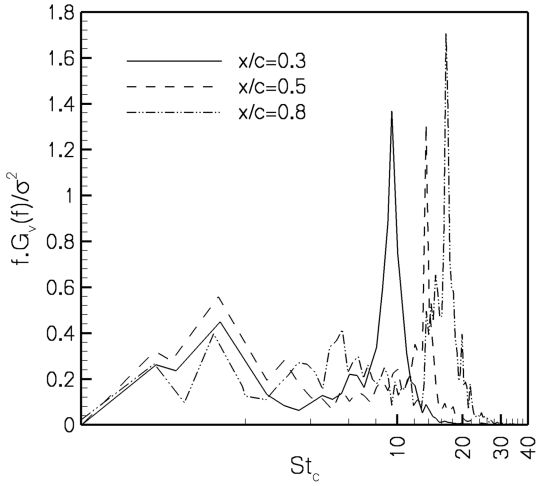

Fig. 6 Spectra of the vertical velocity fluctuations v' for $x/c = 0.3$, 0.5, and 0.9 at the leading edge of the missile fin.

For each spectrum, some characteristic frequencies are discernible. One can observe a high-amplitude peak centered on $St_c = fc/U_\infty = 10$, 14, and 17, respectively, for P_1, P_2. and P_3. According to Table 2, such frequencies have already been found in the literature for flows developing over delta wings. They have always been associated with the Kelvin–Helmholtz instability.

In Fig. 6, two others characteristic frequencies are discernible in the spectra. These frequencies are centered around $St_c = 0.7$ and 1.5. To complement this analysis, Fig. 7 presents cross spectra of pressure on the suction side of the fin recorded at four different numerical probes (P_4 to P_7) beneath the reverse flow.

Because of the high value of the coherence γ around $St_c = 1.5$, it clearly appears that these four probes are subjected to the same phenomenon. To compare the current results with those available in the literature, it is possible to introduce a length scale based on the separation area. The surface of the separated flow is approximately equal to 75% of the surface of the missile fin;, an adequate length scale of the separated flow is $l = \sqrt{0.75 S_{\text{fin}}}$. Based on this new length scale, the nondimensional frequency of the two low-frequency phenomena are $St_l \approx 0.8$ and ≈ 0.37. The value of 0.8 is close to the nondimensional frequency encountered in separated flows in several generic configurations for a Mach number varying from 0.3 to 0.8 and can be associated with the phenomena of vortex-shedding [37]. For $St_l \approx 0.37$, the responsible phenomenon may be identified as the flapping of the shear layer.

This spectral analysis allowed the determination of the natural frequencies of the unforced flow. These frequencies will be further used for setting the pulsing frequencies.

Table 2 Kelvin–Helmholtz frequencies in slender-wing flows

Authors	ψ, deg	α, deg	Re_c	St_c
Gad-el Hak and Blackwelder [34]	45, 60	10, 15	$1, 3–3.5 \times 10^5$,	3–15
Gordnier and Visbal [35,36]	50	25	$2, 6 \times 10^4$	10, 7

V. Study of the Blowing Effects on the Separated Flow

This section presents continuous- and pulsed-blowing effects on the reverse flow over the missile fin. As will be further detailed, the blowing slot is placed all along the leading edge of the fin. The aim of such strategies is to delay the fin stall and then to increase its aerodynamic performance.

A. Presentation of the Control Strategies

Since the flow separates at the leading edge of the fin, the blowing slot has been placed all along the leading edge and the jet is injected perpendicularly to the surface of the fin (see Fig. 8). The blowing velocity and direction are numerically imposed by an injection boundary condition on the upper surface of the fin.

The blowing velocity $v(t)$ follows the following law:

$$v(t) = \frac{V}{2}(1 + \sin(2\pi f t)) \tag{2}$$

where f is the pulsing frequency and V is the maximal velocity amplitude. This velocity is imposed to specify a chosen value of the momentum coefficient C_μ. This coefficient is defined as follows:

$$C_\mu = \frac{\rho_{\text{slot}} S_{\text{slot}} \langle v^2 \rangle}{0.5 \rho_\infty S_{\text{fin}} U_\infty^2} = 1\% \tag{3}$$

where $\langle v \rangle$ refers to the time-averaged blowing velocity. The value of 1% has been chosen for the current investigation. This value approximately corresponds to the maximal value that is experimentally affordable.

The aim of this section is to compare continuous- and pulsed-blowing effects on the separated flow over the fin and to identify an optimal frequency. As presented in Table 3, several pulsing frequencies will be further considered. Note that the nondimensional frequency $F^+ = 1.5$ is associated with that of the natural vortex-

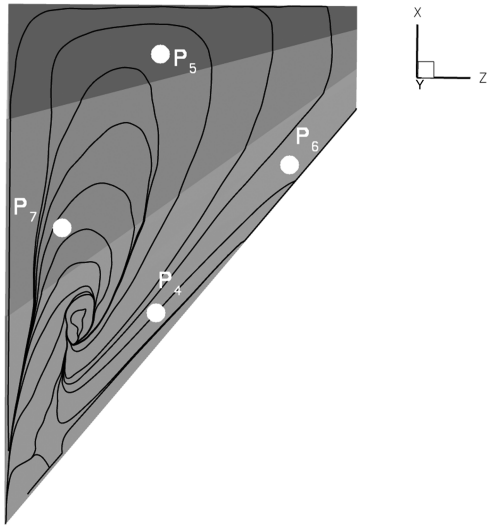

a)

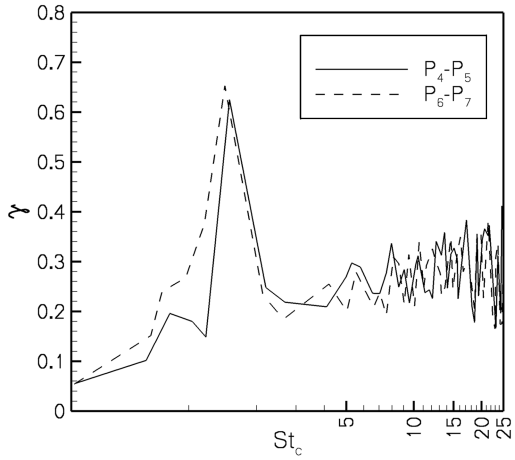

b)

Fig. 7 Cross spectra of wall pressure recorded at the four probes P_5, P_6, P_7, and P_8.

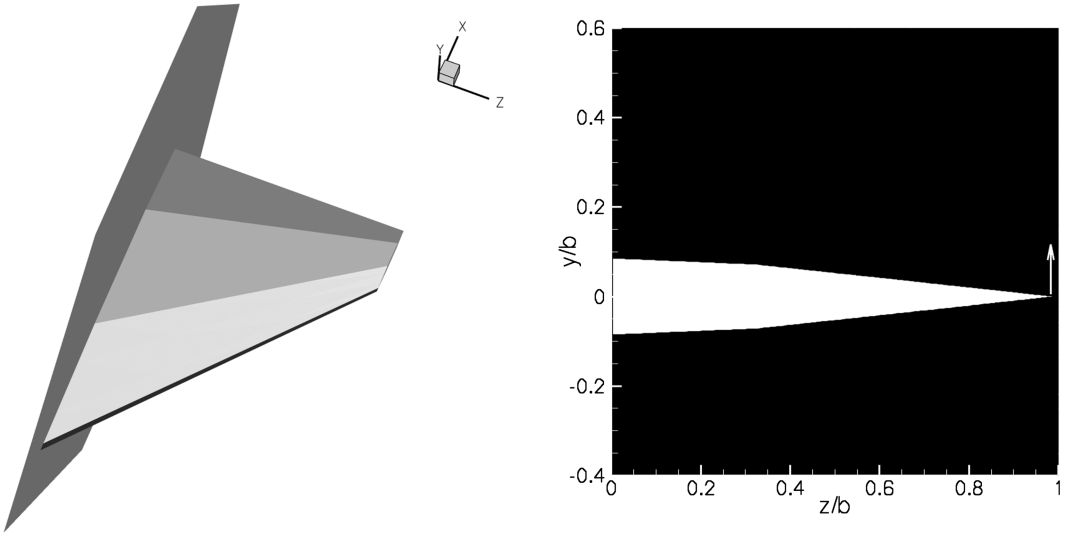

a) b)

Fig. 8 Visualization of the blowing slot (left) and blowing direction (right).

shedding, and $F^+ = 10$ is close to the frequency of the Kelvin–Helmholtz instability.

In the following sections, the continuous-blowing case will be denoted as the $F^+ = 0$ case.

B. Study of the Instantaneous Flows

A first indication of the instantaneous flow behavior due to blowing at the leading edge is given by Fig. 9, presenting an isosurface of $Q = 400 \times U_\infty^2/c^2$ for $F^+ = 0$, 1.5, and 10. The reader can refer to Fig. 4, which shows the same isosurface as in the reference case. In the $F^+ = 0$ case, blowing has a dramatic effect on the vortical structures embedded in the flow. Indeed, the vortex-shedding occurring at the leading edge of the fin in the reference case is inhibited. It then results in a lack of turbulent structures over the first one-third of the fin.

Before the presentation of the pulsed-blowing effects on the instantaneous flow, note that the snapshots presented in Fig. 9 represent the instantaneous flow during the relaxing phase (i.e., no-blowing phase). For conciseness, only the $F^+ = 1.5$ and 10 cases are presented.

In the $F^+ = 1.5$ case, a vortical structure is generated, due to the blowing (denoted by the black dashed line). This structure is then convected in the separated flow in a direction perpendicular to the leading edge of the fin. An interesting feature of the instantaneous flow in this case is the lack of turbulent structures near the vertical plate, in comparison with the unforced case. It may indicate a decrease of the separated-flow size. As observable in Fig. 9c, increasing the blowing frequency leads to a decrease of the size of the vortical structures resulting from the pulsed blowing (see the black dashed lines). Moreover, in the $F^+ = 10$ case, the instantaneous flow appears to be similar to the reference flow, since this pulsing frequency is close to that of the natural Kelvin–Helmholtz instability. Nevertheless, one can note that as for $F^+ = 1.5$, there are less vortical structures along the vertical plate than in the reference instantaneous flow.

Table 3 Overview on the control strategies

Strategy	F^+	Maximal blowing velocity	C_μ
Continuous blowing	0	98.6 m · s^{-1} ($0.4U_\infty$)	1%
Pulsed blowing	1	161 m · s^{-1} ($0.7U_\infty$)	1%
Pulsed blowing	1.5	161 m · s^{-1} ($0.7U_\infty$)	1%
Pulsed blowing	3	161 m · s^{-1} ($0.7U_\infty$)	1%
Pulsed blowing	6	161 m · s^{-1} ($0.7U_\infty$)	1%
Pulsed blowing	10	$161 m.s^{-1}$ ($0.7U_\infty$)	1%

C. Blowing Effects on the Time-Averaged Flow

1. *Blowing Effects on the Reverse Flow*

To illustrate the blowing effects on the time-averaged separated flow, Fig. 10 shows contours of the pressure coefficient C_p on the suction side of the fin and the flow-reattachment line (denoted by the white dashed line). First, it should be emphasized here that the sliverlike decreases of pressure on the suction side at $x/c = 0.4$ and 0.8 are the consequence of the bilosangic airfoil shape.

In the continuous-blowing case, Fig. 10 shows an increase of C_p all over the suction side of the fin. For $F^+ = 1$, a low-pressure region is generated between $x_c = 0.6$ and 0.8, and the pressure in the region of the apex of the missile fin also decreases. The situation for $F^+ = 1.5$ is somewhat similar, even if the low-pressure area progresses toward the apex and both its intensity and size increase. The situation for the three other pulsed cases differs from the first two cases. Indeed, these three strategies have only a favorable effect on the pressure distribution at the fin apex; the large low-pressure zone highlighted in the two previous cases is no longer present. Moreover, it is anticipated that from $F^+ = 3$ to 10, the flow control efficiency will decrease, since the size of the low-pressure area at the apex of the fin and its intensity decrease.

Figure 10 also gives some information about the spatial extent of the separated flow developing over the fin. On one hand, applying continuous blowing at the leading edge of the fin results in a larger reverse-flow region, with the reattachment line moving toward the vertical plate. On the other hand, the separated-flow surface decreases with pulsed blowing, whatever the frequency. Finally, it appears that, as in the case of an airfoil [38–40], the size of the reverse flow decreases when the blowing frequency increases. Finally, for any F^+ values from 0 to 10, the flow is no longer detached at the apex of the fin.

Quantitatively, Table 4 gives the ratio of S/S_{fin} for each case, where S is the surface of the separated flow over the pressure side of the fin (for which the surface equals S_{fin}).

Whereas the continuous-blowing case leads to an increase of S by 5% in comparison with the reference case, S decreases for all of the pulsed-blowing cases, from 10% in the $F^+ = 1$ case to 70% for $F^+ = 10$.

In conclusion to this part of the study, it appears that high-frequency forcing cases are the most efficient for decreasing the size of the separated flow over the fin, but applying low-frequency pulsed blowing is an efficient way to decrease wall pressure on the suction side of the fin.

2. *Blowing Effects on the Aerodynamic Performance of the Missile Fin*

Figure 11 presents the evolution of the lift coefficient C_L and the drag coefficient C_D as functions of the pulsing frequency F^+.

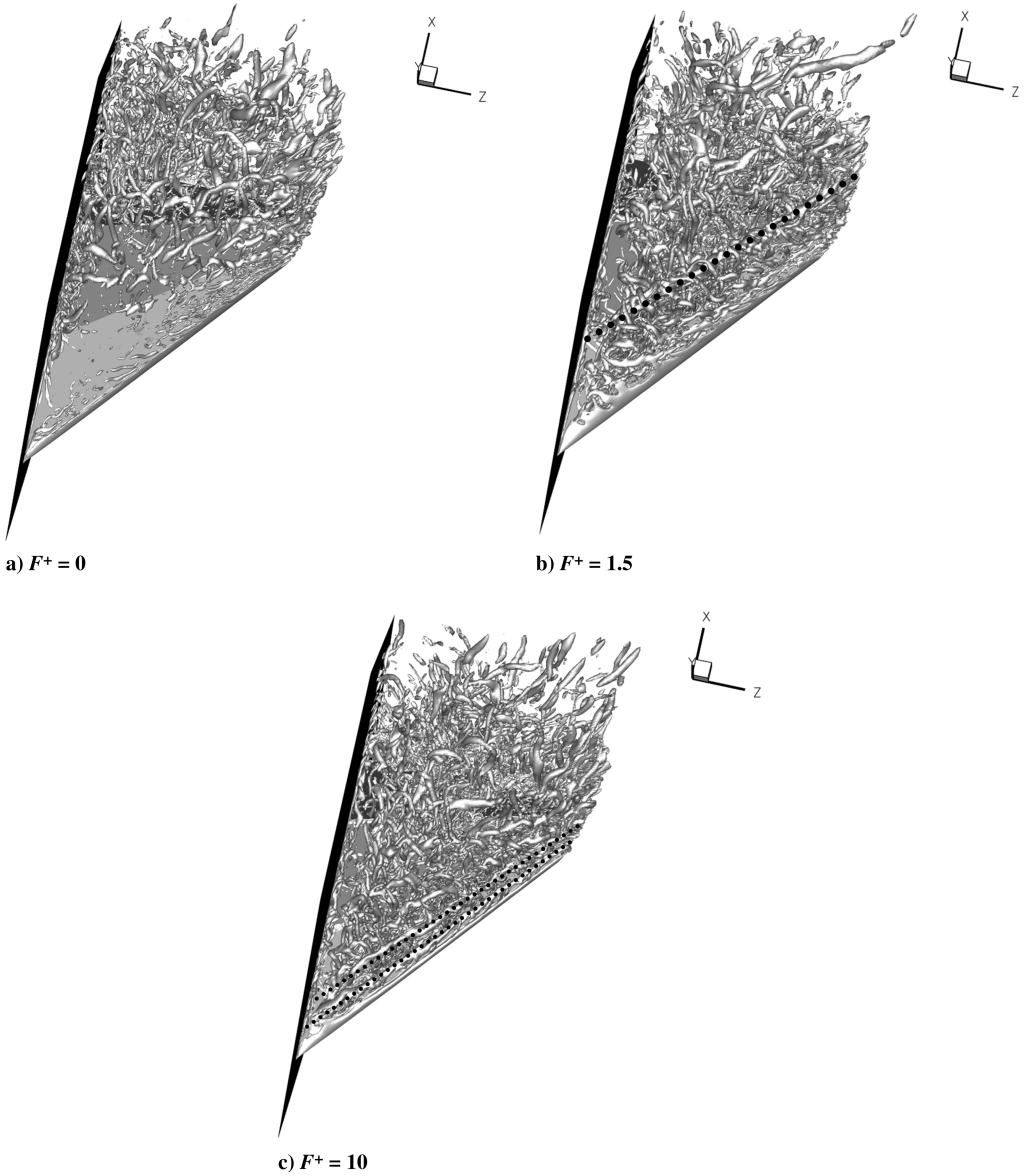

a) $F^+ = 0$ b) $F^+ = 1.5$

c) $F^+ = 10$

Fig. 9 Isosurface of $Q = 400 \times U_\infty^2/c^2$. The dotted lines represent the vortical structures generated by the pulsed blowing.

As expected from the previous observations, the $F^+ = 0$ case alters the aerodynamic performance of the missile fin, since the lift coefficient decreases by 8%. The situation differs for all of the pulsed-blowing cases. Indeed, the lift coefficient increases from $F^+ = 1$ to 1.5 to reach 1.025, representing an improvement of 23.5% in comparison with the reference case. Finally, from $F^+ = 1.5$ to 10, the lift coefficient progressively decreases toward 0.865 (+3.5%). Concerning the drag coefficient, C_D decreases for all of the five pulsed cases, but the most efficient case is once again the $F^+ = 1.5$ case (−42%). It suggests that decreasing the wall pressure on the suction side of the fin is more efficient than decreasing the surface of the separated flow in order to enhance the aerodynamic performance of the fin.

Note that the optimal blowing frequency corresponds to the frequency of the natural vortex-shedding. This suggests that blowing at $F^+ = 1.5$ excites this phenomenon. Such results have been already found in the case of bidimensional shear layers [41]. Moreover, in their study of pulsed-blowing effects on the reverse flow over a 50 deg delta wing, Williams et al. [14] have also found an optimal frequency equal to $F^+ = 1.5$. Additionally, Gursul et al. [42] have applied sinusoidal rolling and pitching motion to some low-sweep delta wings and they showed that the optimal frequency of such movements is close to $St_c = 1.5$. It appears then that exciting the reverse flow with a frequency close to that of the natural vortex-shedding phenomenon is a generic way to control flow separation.

3. Discussion

As previously presented, applying continuous and pulsed blowing leads to the acceleration of the longitudinal flow in the region of the apex of the fin, with the longitudinal velocity component becoming positive. Nevertheless, contrary to the works of Williams et al. [14], it does not lead to the reformation of a leading-edge vortex. The difference in the Reynolds number between our study and that of Williams et al. [14] may explain this observation. Indeed, it has been experimentally demonstrated that the vortical flow developing over moderately swept wings depends on the Reynolds number [43,44], contrary to slender wings ($\psi > 65°$). In fact, an increase of the Reynolds number induces a faster vortex breakdown and the disorganization of the leading-edge vortex. In our study, the Reynolds number based on the root chord of the wing equals 5.8×10^6, whereas it is equal to 2×10^5 in the experimental works of Williams et al. [14]. One can then assume that the regeneration of the leading-edge vortex is more difficult in our case than in the study of Williams et al.

VI. Comparison of Pulsed Blowing and Synthetic Jet

To assess the suction effect on the reverse flow over the fin, the following section is dedicated to the comparison between synthetic jet (which is characterized by a periodic suction and blowing forcing) and pulsed-blowing effects on the reverse flow developing over the

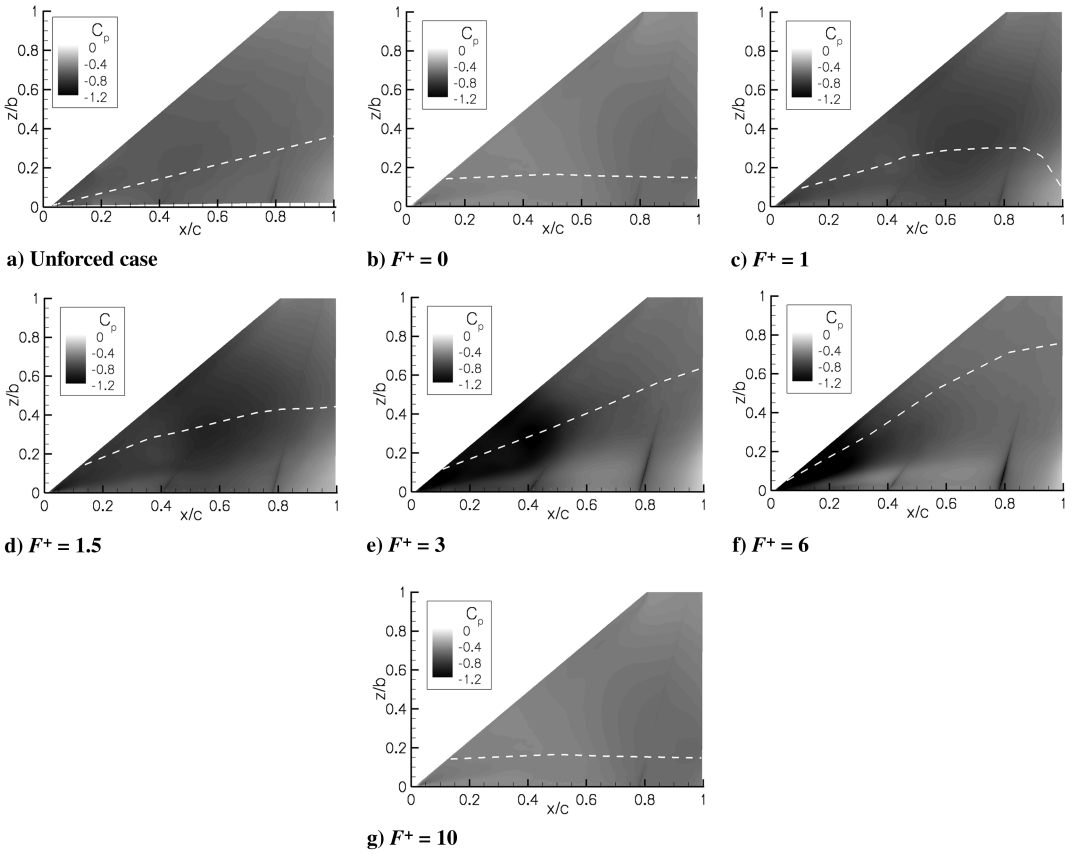

Fig. 10 Contours of C_p on the suction side of the fin and reattachment line (the separated flow is confined between the leading edge of the fin and the white dashed line).

Table 4 Evolution of S/S_{fin} as a function of F^+

Case	Value
Reference case	0.75
$F^+ = 0$	0.79
$F^+ = 1$	0.67
$F^+ = 1.5$	0.59
$F^+ = 3$	0.47
$F^+ = 6$	0.28
$F^+ = 10$	0.22

fin and on its aerodynamic performance. In the case of the synthetic jet, the velocity is given by

$$v(t) = V \times \sin(2\pi \text{ft}) \tag{4}$$

For the two cases, $F^+ = 15$, since it is the optimal frequency identified in the case of a pulsed blowing.

A. Phase-Averaged Flows

To understand the effects of a synthetic jet on the separated flow, let us study the phase-averaged flows. To this end, the forcing cycle has been divided into four phases, and the maximum blowing is located at $\varphi = \pi/2$. Figure 12 presents the evolution of the isocontour $C_p = -1$ in a plane perpendicular to the leading edge at $x_c = 0.5$.

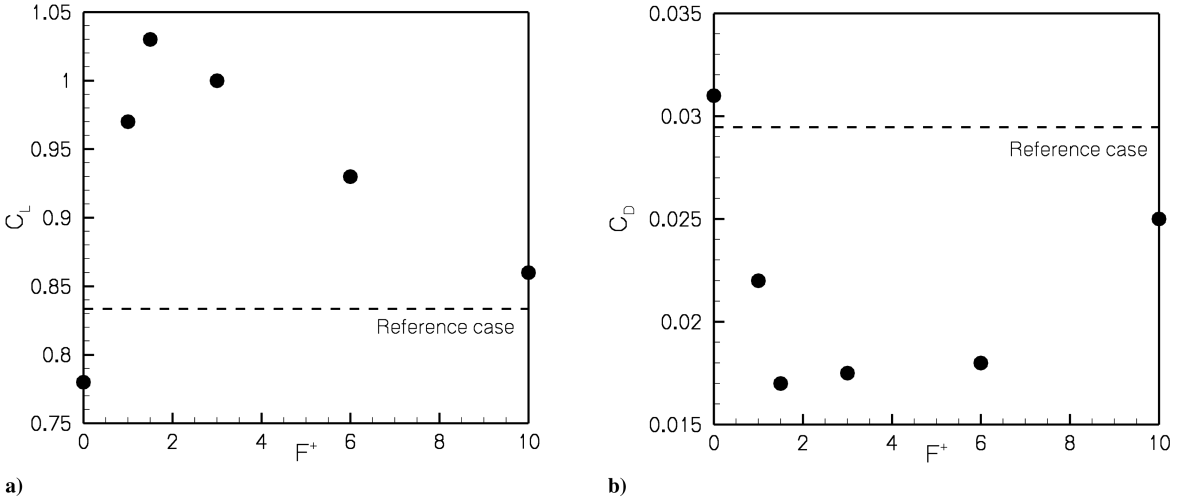

Fig. 11 Blowing effects on the lift (left) and on the drag (right) coefficients.

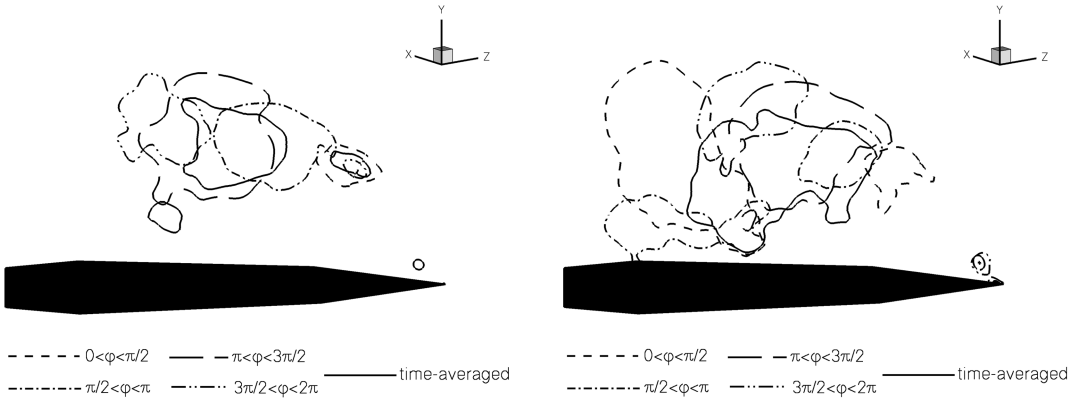

a) Pulsed blowing **b) Synthetic jet**

Fig. 12 Phase- and time-averaged isocontours of $C_p = -1$.

Table 5 Aerodynamic performance of the fin with a pulsed blowing and a synthetic jet at its leading edge

	C_L	C_D
Pulsed blowing	1.021	0.0168
Synthetic jet	1.086	0.008

Table 6 Loading fluctuations

	$(C_L)_{\text{rms}}/C_L$	$(C_D)_{\text{rms}}/C_D$
Reference case	0.01	0.04
Pulsed blowing	0.017	0.13
Synthetic jet	0.02	0.25

In the two cases, this contour permits the identification of a low-pressure structure convecting over the suction side of the fin. It appears in the synthetic-jet case that this structure is closer to the surface of the fin than in the pulsed-blowing case. Although this structure moves away from the fin and its size decreases during the relaxing phase of the pulsed blowing, it is maintained close to the suction side of the fin for $\pi < \varphi < 2\pi$ in the synthetic-jet case. When the following blowing cycle starts, this structure moves toward the surface of the fin while a new one is generated. In other words, using a synthetic jet allows keeping a low-pressure structure close to the suction side of the fin over all the forcing cycle, contrary to the pulsed blowing, and then decreasing the time-averaged pressure coefficient.

B. Synthetic-Jet Effects on the Performance of the Fin

As summarized in Table 5, using a synthetic jet results in an improvement of the aerodynamic performance of the missile fin.

The lift coefficient C_L increases by 30% in comparison with the unforced case (+6.3% in comparison with the pulsed blowing) and the drag coefficient C_D is decreased by 265% (−52% with respect to pulsed blowing).

As presented in Fig. 13, applying pulsed blowing or a synthetic jet leads to an increase of k/U_∞^2, where k is the turbulent kinetic energy, and a displacement of its maxima toward the leading edge of the fin, in comparison with the unforced case. This is particularly true in the case of the synthetic jet, due to the dynamic of the vortical structure previously highlighted. The consequence is, as summarized in Table 6, an increase of the loading fluctuations, with the ratio $(C_L)_{\text{rms}}/C_L$ increasing by 70% with the pulsed blowing and by 100% with the synthetic jet, in comparison with the reference case. This increase is more dramatic for $(C_D)_{\text{rms}}/C_D$, since it reaches 225 and 525%, respectively, for the pulsed and synthetic actuations. Thus, even if the absolute values of the loading fluctuations remain acceptable with the pulsed blowing and the synthetic jet, this parameter should be considered by missile-fin designers.

VII. Conclusions

This study aimed at controlling the separated flow over a moderately swept missile fin, which can be considered as a 50 deg sweep delta wing. The first part of the study was dedicated to the validation and study of the baseline case. The reference simulation allows an accurate prediction of the pressure coefficient repartition according to the available experimental data, and the numerically predicted aerodynamic performance of the fin is in good agreement with the experimentally measured performance. In agreement with the literature, the flow coming from the lower surface of the fin fully separates at its sharp leading edge, and a large region of reverse flow develops on its suction side, resulting in the stall of the fin. The spectral analyses of the resolved vertical fluctuations in the shear layer and those of the wall pressure on the suction side of the fin allow

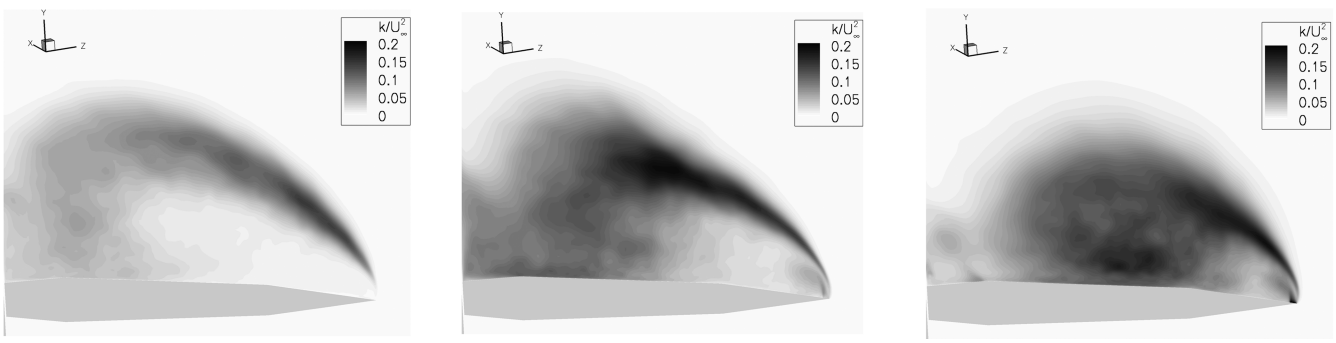

a) Reference case **b) Pulsed blowing** **c) Synthetic jet**

Fig. 13 Contours of k/U_∞^2 in a plane perpendicular to the leading edge of the fin.

identification of frequencies of the natural unsteady phenomena, which are the Kelvin–Helmholtz instability and the vortex-shedding. To control the separated flow, continuous and pulsed blowing have been applied all along the leading edge of the fin. For pulsed blowing, the frequencies based on the freestream velocity and the root chord are $F^+ = 1$, 1.5 (identified as the frequency of the natural vortex-shedding), 3, 6, and 10 (close to the frequency of the Kelvin–Helmholtz instability). Applying continuous blowing results in a larger reverse-flow area than in the reference case and in a delay in the reattachment of the shear layer. As a consequence, the fin aerodynamic performance is deteriorated. Conversely, it has been demonstrated that applying pulsed blowing is an efficient way to control the flow separation over the fin. Indeed, it allows a decrease of pressure on its suction side and of the surface of the separated flow. An optimal frequency has been identified and corresponds to that experimentally observed for lower Reynolds and Mach numbers than in our study.

Finally, a comparison between a synthetic jet and pulsed blowing at $F^+ = 1.5$ has been carried out. In the two cases, a low-pressure structure is generated during the blowing phase, but it is larger and closer to the fin in the synthetic-jet case than with pulsed blowing. During the second phase of the cycle, this structure is dissipated in the pulsed-blowing case, whereas it is sucked toward the suction side of the fin for the synthetic jet. As a consequence, time-averaged pressure levels over the fin are lower with the synthetic jet, and the control efficiency is improved.

Acknowledgment

The authors would like to acknowledge the French Ministry of Defense for its financial support.

References

[1] Mitchell, A. M., "Caractérisation et Contrôle de l'Éclatement Tourbillonnaire sur une Aile Delta aux Hautes Incidences," Ph.D. Thesis, University Paris 6, Paris, 2000.

[2] Renac, F., "Contrôle Expérimental de l'Écoulement Tourbillonnaire sur une Aile Delta," Ph.D. thesis, University Paris 6, Paris, 2004.

[3] Polhamus, E. C., "A Concept of the Vortex Lift of Sharp-Edged Delta Wings Based on a Leading Edge-Suction Analogy," NASA TN D-3767, 1966.

[4] Lee, M., and Ho, C. M., "Lift Force of Delta Wings," *Applied Mechanics Reviews*, Vol. 43, 1990, pp. 209–221.

[5] Escudier, M., "Vortex Breakdown: Observations and Explanations," *Progress in Aerospace Sciences*, Vol. 25, 1988, pp. 189–229. doi:10.1016/0376-0421(88)90007-3

[6] Hall, M. G., "Vortex Breakdown," *Annual Review of Fluid Mechanics*, Vol. 4, 1972, pp. 195–218. doi:10.1146/annurev.fl.04.010172.001211

[7] Leibovich, S., "Vortex Stability and Breakdown: Survey and Extension," *AIAA Journal*, Vol. 22, 1984, pp. 1192–1206. doi:10.2514/3.8761

[8] Earnshaw, P. B., and Lawford, J. A., "Low-Speed Wind-Tunnel Experiments on a Series of Sharp-Edged Delta Wings," ARC Reports and Memoranda No. 3424, 1964.

[9] Wentz, W. H., and Kohlman, D. L., "Vortex Breakdown on Slender Sharp-Edged Wings," *Journal of Aircraft*, Vol. 8, 1971, pp. 156–161. doi:10.2514/3.44247

[10] Miau, J. J., Kuo, K. T., Liu, W. H., Hsieh, S. J., Chou, J. H., and Lin, C. K., "Flow Developments Above 50-Deg Sweep Delta Wings with Different Leading-Edges Profiles," *Journal of Aircraft*, Vol. 32, 1995, pp. 787–794. doi:10.2514/3.46792

[11] Ol, M. V., and Gharib, O., "The Passage Toward Stall of Nonslender Delta Wings at Low Reynolds Number," AIAA Paper 2001-2843, 2001.

[12] Ol, M. V., and Gharib, O., "Leading-Edge Vortex Structure of Nonslender Delta Wings at Low Reynolds Number," *AIAA Journal*, Vol. 41, 2003, pp. 16–26. doi:10.2514/2.1930

[13] Rullan, J., Vlachos, P. P., and Telionis, D. P., "Aerodynamics and Flow Control over Swept Wings and Wings with Diamond Planform," AIAA Paper 2007-879, 2007.

[14] Williams, N. M., Wang, Z., and Gursul, I., "*Active Flow Control on a Nonslender Delta Wing*," AIAA Paper 2008-740, 2008.

[15] Spalart, P. R., Deck, S., Shur, M. L., Squires, K. D., Strelets, M. K., and Travin, A., "A New Version of Detached-Eddy Simulation, Resistant to Ambiguous Grid Densities," *Theoretical and Computational Fluid Dynamics*, Vol. 20, 2006, pp. 181–195. doi:10.1007/s00162-006-0015-0

[16] Deck, S., "Zonal Detached Eddy Simulation of the Flow Around a High Lift Configuration," *AIAA Journal*, Vol. 43, No. 11, 2005, pp. 2372–2384. doi:10.2514/1.16810

[17] Riou, J., Garnier, E., Deck, S., and Basdevant, C., "Improvement of Delayed-Detached Eddy Simulation Applied to Separated Flow over Missile Fin," *AIAA Journal*, Vol. 47, No. 2, 2009, pp. 345–360. doi:10.2514/1.37742

[18] Fargier, T., "Essai de Pesées et de Mesure PSP sur la Gouverne MATRA $n°11$ dans la Veine Transsonique de la Soufflerie S3MA," ONERA, Modane, France, 2003.

[19] Pechier, M., "Prévisions Numériques de l'Effet Magnus Pour des Configurations de Munition," Ph.D. Thesis, University Paris 6, Paris, 1999.

[20] Gear, C. W., "Algorithm 407-DIFSUB for the Solution of Ordinary Differential Equations," *Communications of the ACM*, Vol. 14, 1971, pp. 185–190. doi:10.1145/362566.362573

[21] Mary, I., Sagaut, P., and Deville, M., "An Algorithm for Low Mach Number Unsteady Flows," *Computers and Fluids*, Vol. 29, 2000, pp. 119–147. doi:10.1016/S0045-7930(99)00007-9

[22] Mary, I., and Sagaut, P., "Large Eddy Simulation of the Flow Around an Airfoil Near Stall," *AIAA Journal*, Vol. 40, 2002, pp. 1139–1146. doi:10.2514/2.1763

[23] Deck, S., Garnier, E., and Guillen, P., "Turbulence Modeling Applied to Space Launcher Configurations," *Journal of Turbulence* [online journal], Vol. 3, No. 1, 2002, Paper N 57. doi:10.1088/1468-5248/3/1/057

[24] Deck, S., and Thorigny, P., "Unsteadiness of an Axisymmetric Separating-Reattaching Flow: Numerical Investigation," *Physics of Fluids*, Vol. 19, 2007, Paper 065103. doi:10.1063/1.2734996

[25] Simon, F., Deck, S., Guillen, P., Sagaut, P., and Merlen, A., "Numerical Simulation of the Compressible Mixing Layer Past an Axisymmetric Trailing Edge," *Journal of Fluid Mechanics*, Vol. 591, 2007, pp. 215–253.

[26] Larchevêque, L., Labbé, O., Mary, I., and Sagaut, P., "Large-Eddy Simulation of a Compressible Flow Past a Cavity," *Physics of Fluids*, Vol. 15, 2003, pp. 193. doi:10.1063/1.1522379.

[27] Dandois, J., Garnier, E., and Sagaut, P., "Unsteady Simulation of Synthetic Jet in a Crossflow," *AIAA Journal*, Vol. 44, 2006, pp. 225–238. doi:10.2514/1.13462

[28] Dandois, J., Garnier, E., and Sagaut, P., "DNS/LES of Active Separation Control," *Journal of Fluid Mechanics*, Vol. 574, 2007, pp. 25–58. doi:10.1017/S0022112006003995

[29] Spalart, P. R., and Allmaras, S. R., "A One-Equation Turbulence Model for Aerodynamic Flows," AIAA Paper 1992-04339, 1992.

[30] Riou, J., Garnier, E., and Basdevant, C., "Compressibility Effects on the Vortical Flow over a 65° Sweep Delta Wing," *Physics of Fluids*, Vol. 22, No. 3, 2010, Paper 035102. doi:10.1063/1.3327286

[31] Riou, J., Garnier, E., and Basdevant, C., "Control of the Flow over a Delta Wing in the Transonic Regime," *AIAA Journal*, Vol. 48, No. 8, 2010, pp. 1851–1855. doi:10.2514/1.J050531

[32] Jeong, J., and Hussain, F., "On the Identification of a Vortex," *Journal of Fluid Mechanics*, Vol. 285, 1995, pp. 69–94. doi:10.1017/S0022112095000462

[33] Welch, P. D., "The Use of Fast Fourier Transform for the Estimation of Power Spectra: A Method Based on Time Averaging over Short Modified Periodograms," *IEEE Transactions on Audio and Electroacoustics*, Vol. 15, 1967, pp. 70–73. doi:10.1109/TAU.1967.1161901

[34] Gad-el Hak, M., and Blackwelder, R. F., "The Discrete Vortices from a Delta Wing," *AIAA Journal*, Vol. 23, No. 6, 1985, pp. 961–962. doi:10.2514/3.9016

[35] Gordnier, R. E., and Visbal, M. R., "Compact Difference Scheme Applied to Simulation of Low-Sweep Delta Wing Flow," *AIAA Journal*, Vol. 43, 2005, pp. 1744–1752. doi:10.2514/1.5403

[36] Gordnier, R. E., and Visbal, M. R., "Computational and Experimental Investigation of a Nonslender Delta Wing," AIAA Paper 2007-894,

2007.
[37] Mabey, D. G., "Analysis and Correlation of Data on Pressure Fluctuations in Separated Flow," *Journal of Aircraft*, Vol. 9, No. 9, 1972, pp. 642–645.
doi:10.2514/3.59053
[38] Glezer, A., Amitay, M., and Honohan, A. M., "Aspects of Low- and High-Frequency Actuation for Aerodynamic Flow Control," *AIAA Journal*, Vol. 43, No. 7, 2005, pp. 1501–1511.
doi:10.2514/1.7411
[39] Amitay, M., and Glezer, A., "Role of Actuation Frequency in Controlled Flow Reattachment over Stalled Airfoil," *AIAA Journal*, Vol. 40, No. 2, 2002, pp. 209–216.
doi:10.2514/2.1662
[40] Amitay, M., Horvath, M., Michaux, M., and Glezer, A., "Virtual Aerodynamic Shape Modification at Low Angles of Attack Using Synthetic Jet Actuators," AIAA Paper 2001-2975, 2001.
[41] Chun, K. B., and Sung, H. J., "Control of Turbulent Separated Flow over a Backward-Facing Step," *Experiments in Fluids*, Vol. 21, 1996, pp. 417–426.
[42] Gursul, I., Vardaki, E., and Wang, Z., "Active and Passive Control of Reattachment on Various Low-Sweep Wings," AIAA Paper 2006-506, 2006.
[43] Visbal, M. R., and Gordnier, R. E., "Higher-Order Compact Difference Scheme Applied to the Simulation of a Low Sweep Delta Wing Flow," AIAA Paper 2003-620, 2003.
[44] Gursul, I., "Review of Unsteady Vortex Flows over Slender Delta Wings," *Journal of Aircraft*, Vol. 42, No. 2, 2005, pp. 299–319.
doi:10.2514/1.5269

J. Sahu
Associate Editor